Physical origin of the ferromagnetic ordering above room temperature in GaMnN nanowires

2005 J. Phys.: Condens. Matter 17 5073

(http://iopscience.iop.org/0953-8984/17/33/011)

INSTITUTE OF PHYSICS PUBLISHING JOURNAL OF PHYSICS: CONDENSED MATTER

J. Phys.: Condens. Matter **17** (2005) 5073–5085 doi:10.1088/0953-8984/17/33/011

Physical origin of the ferromagnetic ordering above room temperature in GaMnN nanowires

Y P Song[1], P W Wang[1], H Q Lin[2], G S Tian[1], J Lu[1], Z Wang[1], Y Zhang[1] and D P Yu[1,3]

[1] Electron Microscopy Laboratory and State Key Laboratory of Mesoscopic Physics, Department of Physics, Peking University, Beijing 100871, People's Republic of China
[2] Department of Physics, The Chinese University of Hong Kong, Shatin, New Territory, Hong Kong, China

Received 4 June 2005
Published 5 August 2005
Online at stacks.iop.org/JPhysCM/17/5073

Abstract

We report a new method for large-scale production of GaMnN nanowires, by annealing manganese–gallium oxide nanowires in flowing ammonia at high temperature. Microstructure analysis indicates that the GaMnN nanowires have wurtzite GaN structure without Mn precipitates or Mn-related second phases. Magnetic measurements reveal that ferromagnetic ordering exists in the GaMnN nanowires, whose Curie temperature is above room temperature. A mean-field model based on the exchange coupling of the nondegenerate carrier-localized impurity band, together with the consideration of the superexchange antiferromagnetic interaction, is used to explain the physical origin of the observed ferromagnetic ordering. Theoretical calculations indicate that the Curie temperature increases with the increase of the hole density and reveal a small ratio of the hole to the magnetic dopant density in the samples. The low ratio of hole to Mn concentration and the superexchange antiferromagnetic interaction lead to the very concave temperature dependence of the magnetization curve in contrast to conventional ferromagnetic M–T behaviour. The theoretical calculation is in agreement with the experimental data.

Recently, diluted magnetic semiconductors (DMSs) have attracted considerable attention since they manifest both the spin and charge properties of the carriers, and much effort has been devoted to spintronics from the viewpoint of fundamental physics and potential applications. A high-Curie-temperature DMS above room temperature is the key for applications. A breakthrough theoretical work reported that some wide-bandgap semiconductors such as GaN and ZnO are the most promising candidates for achieving practical ferromagnetic ordering with T_c above room temperature [1, 2]. Much work has then focused on the Mn-based II–VI and III–V semiconductor materials, such as GaMnAs, InMnAs, GaMnN and

[3] Author to whom any correspondence should be addressed.

ZnMnO etc [3–6]. GaMnAs is found to be ferromagnetic with a Curie temperature around 110 K [7]. Ferromagnetic ordering in Mn-doped GaN has also stimulated intensive research interest [5, 8, 9] because GaN is a wide-bandgap semiconductor with promising optical and electric properties. Reed *et al* reported ferromagnetism in GaMnN films in the temperature range 228–370 K [10]. Ferromagnetism above room temperature was also observed in GaMnN films grown by MBE with Mn contents of 6–9 at.% [11]. Katayama-Yoshida *et al* [12] calculated the electronic structure of transition element (Mn, Fe or Co) doped GaN based on local spin density functional formalism, and found that $Ga_{0.75}Mn_{0.25}N$ has stable ferromagnetic states. However, preparation of a III–V DMS with a high concentration of magnetic ions substituting for the cation sites has been a harsh task under conventional growth conditions. The major difficulties have been the low solubility of magnetic elements (such Mn) in semiconducting compounds [13]. It is demonstrated that ferromagnetic ordering can be destroyed if the content of Mn in GaN is larger than 3 at.% because the extra Mn will stay in nonsubstitutional positions, instead of substituting for Ga sites, forming Ga_xMn_y clusters [14]. Also, previous work was concentrated on the magnetic ceramics and films, and few on the nanoscale DMS materials [15]. The greatest challenge to date is to fabricate nanoscale magneto-optical devices and GaMnN DMS nanowires are the most promising materials for such applications. Although GaMnN nanowires have been prepared on a small scale using carbon nanotubes as a template [15], to our knowledge, no report of large-scale preparation of GaMnN nanowires has been made so far. Here, we describe a simple method for large-scale production of GaMnN nanowires, by annealing manganese–gallium oxide nanowires in flowing ammonia at high temperature. We evaluate the evolution process of the ferromagnetic ordering caused by nitrogen doping from Mn-doped β-Ga_2O_3 in flowing ammonia. A mean-field model is used to explain the physical origin of the observed ferromagnetic ordering, with emphasis on the exchange coupling of the *nondegenerate* carrier-localized impurity band, together under consideration of the superexchange antiferromagnetic interaction.

1. Sample preparation

The idea to prepare high-Mn-concentration GaMnN nanowires arises from our recent work. We found that nitrogen doping in Ga_2O_3 nanowires can introduce novel acceptor levels around the middle of the bandgap of the Ga_2O_3 nanowires [16]. It was further found that heavy nitrogen doping can transform the Ga_2O_3 nanowires into GaN nanowires [17]. So we started from preparation of Mn-doped Ga_2O_3 nanowires (GaONWs) using a vapour phase evaporation method [18]. One hundred milligrams of metallic gallium was put on a silicon substrate and placed into a quartz boat. 1.1 g $MnCl_2{\cdot}4H_2O$ powder was placed 10 cm in front of the metallic gallium source and three silicon substrates (110) deposited with 5 nm Au film were placed downstream of the quartz boat. The quartz boat was then put into the center of an alumina tube ($\varnothing$ 6 cm $\times$ 100 cm), which was inserted in a horizontal tube furnace. The furnace was heated to 900 °C and kept for 30 min for nanowire growth in flowing argon at 80 sccm, and then kept directly in flowing ammonia at different temperatures for direct nitrogen doping. When naturally cooled down to room temperature, a yellowish-brown layer material was observed on the substrates. Five samples, named samples A, B, C, D and E, were prepared using this method (sample A, 750 °C/40 min/50 sccm/1.1 g; sample B, 850 °C/40 min/50 sccm/1.2 g; sample C, 950 °C/40 min/50 sccm/1.0 g; sample D, 1050 °C/40 min/100 sccm/0.80 g; sample E, 1050 °C/40 min/100 sccm/1.1 g; sample, annealing temperature/time/ammonia flow/$MnCl_2{\cdot}4H_2O$). The concentration of the manganese was controlled by the amount of the source material ($MnCl_2{\cdot}4H_2O$ powder) and its relative position to the substrates.

2. Structure characterization and composition analysis

The morphology of the products was analysed using scanning electron microscopy (SEM). Figure 2(a) shows the typical SEM image of sample D, which indicates that the products consist mainly of nanowires with diameter ranging from 30 to 120 nm and the typical lengths are in the range between 10 and 50 μm. Furthermore, large-scale production of nanowires can be found on the whole silicon substrate. The bulk quantity of the samples permits us to characterize the structure evolution of the as-grown manganese–gallium oxide nanowires due to nitrogen doping at different temperatures using x-ray diffraction (XRD). Figure 1(a) shows the XRD spectra of the samples. It can be seen that the diffraction patterns from samples A, B and C are characteristic of monoclinic β-Ga_2O_3 phase mixed with $MnGa_2O_4$ spinel phase. It is noteworthy that the diffraction peak around 57.82° corresponding to the GaN $(11\bar{2}0)$ planes appears in samples B and C. With the increase of the heat-treatment temperature, more nitrogen atoms will substitute for the oxygen, and the structure of the products gradually transformed into wurtzite-type GaN phase. For example, there is mainly wurtzite GaN phase in the diffraction pattern for sample D and E. There are several small peaks in the XRD patterns for sample D, which correspond to β-Ga_2O_3 phase. It is possible that some underlayer nanowires are difficult to contact fully with the ammonia atmosphere and not transformed completely into GaN phase at this annealing temperature. It is noted that no diffraction peaks corresponding to Mn precipitates or Mn-related impurity phases were observed for samples D and E. The lattice parameters measured from the XRD data are $a = 3.188$ Å, $c = 5.186$ Å for sample D and $a = 3.190$ Å, $c = 5.189$ Å for sample E respectively. The lattice parameters increase with the increase of the Mn dopant concentration, as shown in figure 1(b), which indicates that the Mn ions systematically substituted for the Ga ions in the crystal lattice without changing the wurtzite structure.

The morphology and microstructure of the products were further characterized in detail using a transmission electron microscope (TEM). Because the GaMnN nanowires are the desired products in our preparation strategy, much attention was paid to samples D and E for their microstructure analysis. The typical low-magnification TEM images of a nanowire from sample D and sample E are shown in figures 2(b) and (c), respectively. The chemical composition was analyzed combining energy-dispersive x-ray spectroscopy (EDS), electron energy loss spectroscopy (EELS) and x-ray photoelectron spectroscopy (XPS). EDS analysis for samples A, B, C, D and E reveals that the nitrogen concentration increases with the increase of the heat-treatment temperature, while the oxygen concentration decreases accordingly. This shows that the nitrogen concentration can be controlled by controlling the annealing temperature, and the higher the heat-treatment temperature the more the nitrogen doped into the nanowires. When the heat-treatment temperature increases to 1050 °C, the nanowires from samples D and E consist of gallium, nitrogen and manganese with trace amounts of oxygen. The Mn concentration is about 4 and 8 at.% for samples D and E respectively (sample D, $Ga_{0.96}Mn_{0.04}N$; sample E, $Ga_{0.92}Mn_{0.08}N$). Although wurtzite GaN phase appears in samples B and C, it is difficult to give the value of the Mn concentration only in the GaN phase because of the multi-phases in the nanowires (β-Ga_2O_3, $MnGa_2O_4$ and GaN phases). However, EDS analysis can give the atom ratio of Mn to Ga and the value is 9, 9 and 6 at.% (Mn/(Mn + Ga)) for samples A, B and C, respectively. Figure 2(d) shows the Ga and Mn elements mapping from a single nanowire in sample A, and it can be seen that the Mn atoms are homogeneously distributed in the nanowire. X-ray photoelectron spectroscopy (XPS) is a powerful method to study the element binding state and the chemical environment in a crystal. It was also used here to analyse the chemical composition in the samples. The XPS spectra of Mn(2p) show the binding energy is 641.19 and 641.66 eV for samples D and E, respectively.

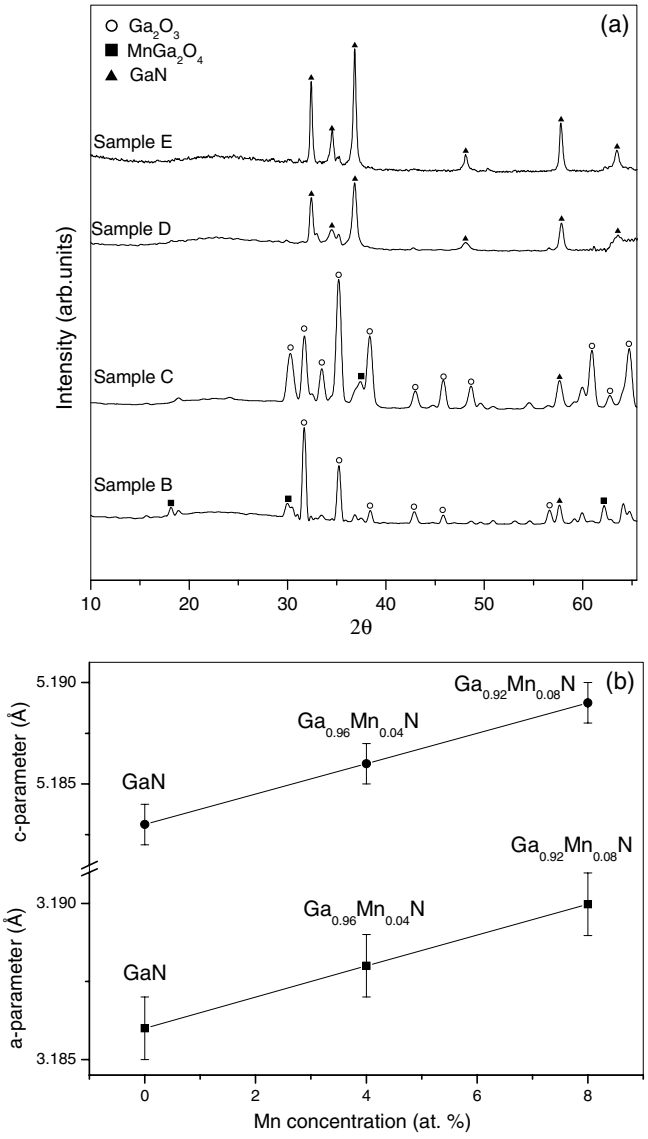

Figure 1. (a) XRD spectrum of samples B, C, D and E. It is visible that the products transform into wurtzite GaN phase when heat-treated at high temperature. (b) The Mn content dependence of the lattice parameters reveals that the lattice parameter increases as the Mn concentration increases in the $Ga_{1-x}Mn_xN$ samples.

According to quantitative XPS analysis, the Mn dopant concentrations for two samples are 4.7 and 8.2 at.%, which are consistent with the EDS analysis. The binding energy of N(1s) is 397.50 and 397.61 eV for samples D and E respectively, which tends to approach that of GaN.

Although XRD analysis reveals that no Mn-related second phase was observed in samples D and E, we cannot exclude the second phase presence completely only using XRD due to the sensitivity limit. Therefore, we further use TEM with electron diffraction and

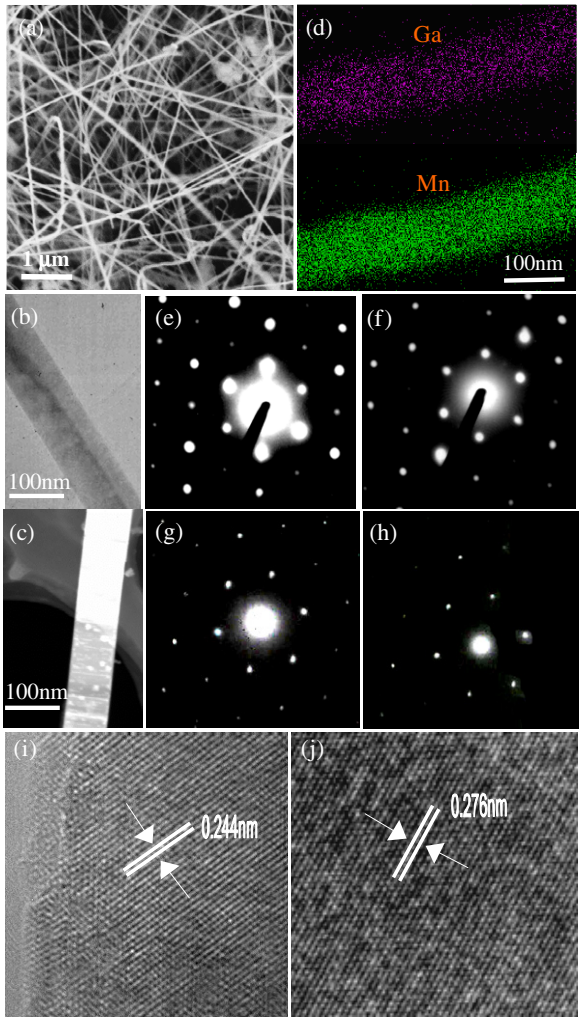

Figure 2. SEM image of sample D (a); TEM images of a single nanowire from sample D (b) and sample E (c); (d) Ga and Mn element mapping in a single nanowire for sample A. It is visible that the Mn element is homogeneously distributed in the nanowire; (e) and (f) show the SAED patterns with both [0001] zone axes for sample D; (g) and (h) show the SAED patterns with both [0001] zone axes for sample E; (i) and (j) show the HRTEM images of a single nanowire from sample D and E. The measured lattice spacing in the image is 0.244 nm for sample D and 0.276 nm for sample E, which correspond to the interplanar spacing of the $(\bar{1}011)$ and $(10\bar{1}0)$ planes of the wurtzite GaN structure respectively.

(This figure is in colour only in the electronic version)

HRTEM experiments to detect the possible second phases in the sample. In TEM methodology, selected area electron diffraction (SAED) and dark-field (DF) imaging analysis are the most useful technique to study if there is any precipitation in the matrix phase. If there is any precipitation among the main phase, there must be some extra (satellite) diffraction spots besides the dominant SAED pattern. Moreover, one can manage to tilt the sample to excite a particular extra diffraction spot intensive enough to form a dark-field image, so that the precipitates will brighten up among the dark background matrix phase. So we extended

these analyses on the region in the samples where the Mn incorporation was presented by EDS analysis. Detailed selected area electron diffraction (SAED) experiments were carried out with selected area close to the diametral range of the nanowire. Figures 2(e), (f) and (g), (h) show the two SAED patterns taken from different nanowires from sample D and sample E respectively. The diffraction patterns show sixfold symmetry without extra diffraction spots, which are identical to the GaN hexagonal structure corresponding to the [0001] zone axis. In order to detect the possible ferromagnetic nanocluster in the local area of the nanowire, a series of electron diffractions is carried out along the axis of the nanowire. However, all SAED patterns show sixfold symmetry with GaN hexagonal structure without extra diffraction spots due to the second phases. Statistical SAED on many individual nanowires for both sample D and sample E did not reveal satellite diffraction spots arising from precipitates, which indicates that either tetragonal (Mn_3N_2, MnN, GaMn, $Ga_{0.4}Mn_{0.6}$) or cubic (Mn_4N, Mn, $Ga_{7.7}Mn_{2.3}$, Ga_5Mn_8) phase can be excluded in the two samples. Mn oxide second phase can also be excluded because no Mn oxide phase has hexagonal structure. The only possible hexagonal phase present could be $GaMn_3$; however, it was not found in XRD analysis. The most important thing is that the lattice parameters of $GaMn_3$ ($a = 5.404$ Å, $c = 4.357$ Å) phase did not match the electron diffraction patterns. The above experiments strongly demonstrate one single GaN phase in samples D and E. The SAED patterns of the nanowire from intermediate products, such as samples A, B and C, appear complex instead of a single one. The detailed analysis indicates that the satellite diffraction spots correspond to the β-Ga_2O_3, $MnGa_2O_4$ and GaN lattice structure, which is consistent with the XRD result. Compared with the single GaN phase in samples D and E, the complex SAED patterns reveal that these intermediate products undergo phase transformation to wurtzite GaN phase when annealing at higher temperature (such as 1050 °C). High-resolution TEM (HRTEM) can provide the insight into the detailed atomic structure of samples D and E. Figures 2(i) and (j) show the HRTEM images of a single nanowire from samples D and E. The images show a clear and structurally perfect surface. The clear lattice fringes in the image indicate a single-crystal structure of the nanowire. The measured lattice spacing in the image is 0.244 nm for sample D and 0.276 nm for sample E, which corresponds to the interplanar spacing of the $(\bar{1}011)$ and $(10\bar{1}0)$ planes of the wurtzite GaN structure respectively. The HRTEM analysis further confirmed that the manganese was doped into the lattice structure instead of being precipitated in samples D and E.

Recently, GaMnN was obtained independently by different methods. Overberg *et al* [19] reported that the GaMnN film with single GaN phase containing 7 at.% Mn was grown by gas source molecular-beam epitaxy (MBE). Theodoropoulou *et al* [8] reported on the magnetic properties of p-GaN with 3–5 at.% Mn concentration grown by metal organic chemical vapour deposition (MOCVD). SAED analysis revealed that the sample has only hexagonal GaN phase. Zajac *et al* [20] prepared microcrystalline GaMnN samples using an ammonothermal method, and x-ray diffraction showed characteristic diffraction lines for hexagonal GaN phase mixed with a small contribution from the Mn_3N_2 phase. We believe that the diversity lattice structure of GaMnN prepared by different methods depends on the growth condition. In our preparation strategy, Mn-doped GaN nanowires were prepared by the two-step method. In the first step, manganese was *in situ* doped into Ga_2O_3 nanowires during nanowire growth, which enables a high amount of manganese to be doped into gallium oxide due to the high solubility of the manganese–gallium oxide system. In the second step, the as-grown manganese–gallium oxide nanostructures were heat-treated in flowing ammonia at different temperatures so that the nitrogen substitutes for oxygen sites, and finally transformed into GaMnN nanowires. Therefore, the manganese atoms were 'frozen' in the Mn-doped GaN structure during the preparation process, preventing aggregation as it does during conventional Mn doping in GaN.

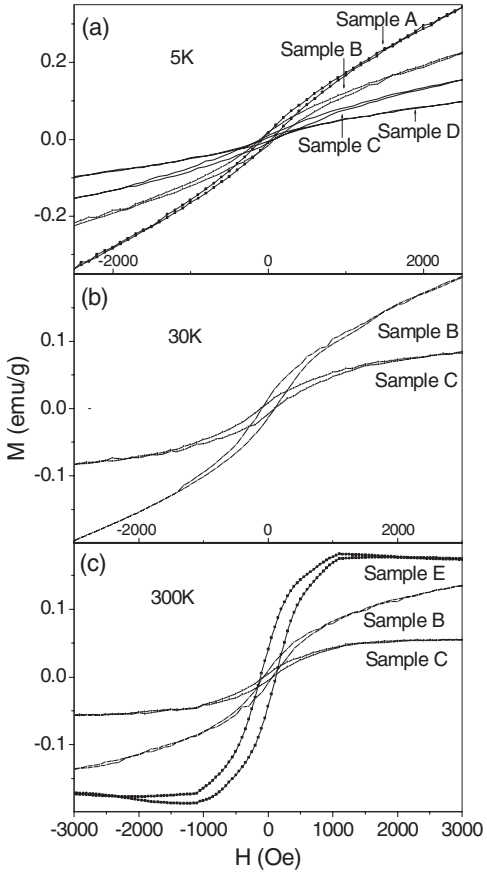

Figure 3. M–H relationship of samples A, B, C, D and E measured at 5, 30 and 300 K, respectively. An obvious hysteresis loop is observed for samples B, C and E above room temperature.

3. Magnetic measurements

The magnetization of the samples was measured using a commercial superconducting quantum interference device (SQUID) magnetometer (Quantum Design, MPMS) to evaluate the evolution process of the magnetic behaviour caused by nitrogen doping. Figure 3 shows the field dependence of magnetization (M–H) for samples A–E at 5, 30 and 300 K respectively, and the applied field is in between −15 000 and 15 000 Oe. At 5 K, there is a hysteresis loop for all samples, as shown in figure 3(a). At 30 K, the hysteresis loop disappears for sample A, while samples B and C have obvious hysteresis loops (figure 3(b)). At 300 K, there still exist obvious hysteresis loops for samples B, C and E, as shown in figure 3(c), which indicates that ferromagnetic ordering exists in these samples above room temperature. The coercive force is 72, 82 and 127 Oe for samples B, C and E respectively. The saturation magnetization per Mn atom is 0.032 μ_B for sample E. Sample D has a small hysteresis loop at room temperature (not shown), which is ascribed to the lower Mn concentration. All of this indicates that the magnetism and Curie temperature are related to the change of the Mn and N concentration in the sample, and the higher concentration of Mn and N leads to enhanced ferromagnetism. The temperature dependence of the magnetization (M–T) is also measured during the field-cooling process under a magnetic field of 500 Oe for all the samples. The scatter curve in figure 4(c) shows the M–T curve for sample E. The magnetization shows a slight increase from 300 to 80 K, followed by a steep increase below 50 K to the measurement limit temperature 5 K. The

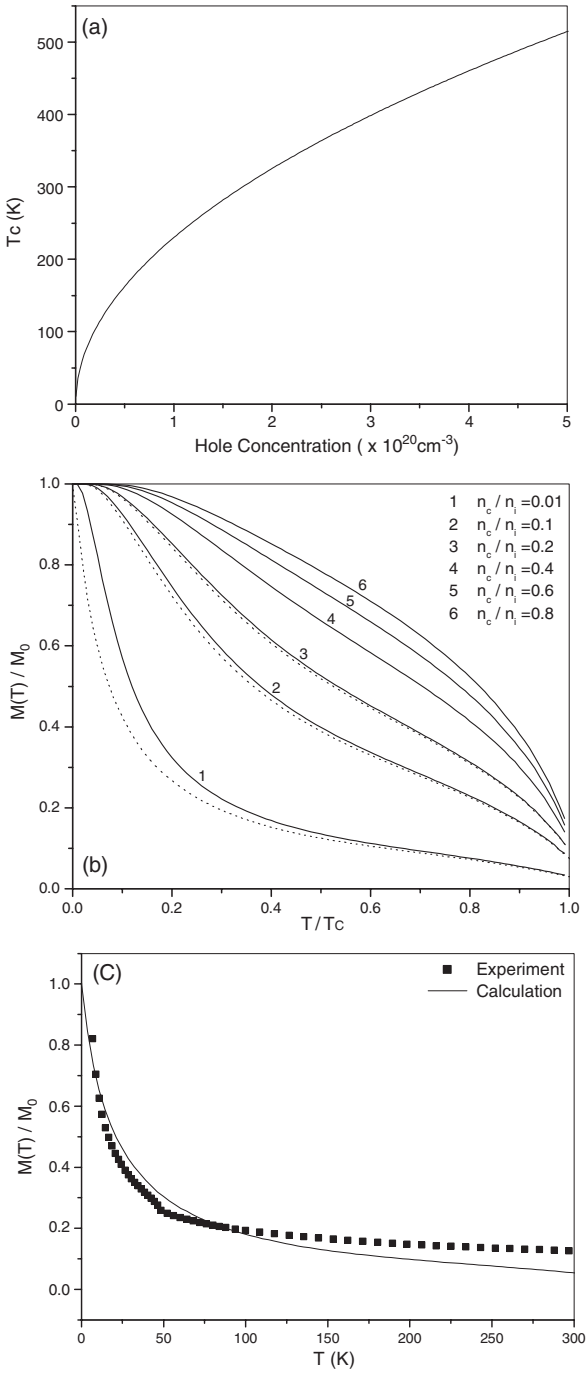

Figure 4. (a) Calculated T_c as a function of the hole concentration for $Ga_{0.95}Mn_{0.05}N$. (b) Spontaneous magnetization $M(T)/M_0(H = 0)$ with $S = 5/2$ and $s = 1/2$ from the nondegenerate-hole model for $Ga_{0.95}Mn_{0.05}N$ with various values of density ratio (n_c/n_i = 0.01, 0.1, 0.2, 0.4, 0.6, 0.8). Dashed curves are the magnetization curves under consideration of the antiferromagnetic surperexchange with $Z^{AF}J^{AF}/\beta N_0 = 8 \times 10^{-5}$, 1×10^{-4}, 1×10^{-4} for $n_c/n_i = 0.01$, 0.1 and 0.2, respectively. (c) Magnetization calculation result compared with the experimental data for sample E.

experimental M–T curve exhibits an untypical outwardly concave shape, significantly different from the usual convex M–T behaviour for conventional ferromagnetic materials. Due to the measurement limit, the magnetization can be only measured below 300 K. No Curie change point is found in that temperature range. However, the magnetization measurement proves the Curie temperature is above the room temperature for sample E.

Recently, stable Mn_4N ferrimagnetic phase was reported to have a T_c as high as 745 K [21]. GaMn ferromagnetic crystallites were also reported to have T_c above room temperature [8]. It may be inferred that the segregation of those ferromagnetic compounds is an origin of the high T_c ferromagnetism in Mn-doped GaN materials. However, we believe that the ferromagnetism in the GaMnN nanowire samples (samples D and E) originates from the GaMnN rather than the ferromagnetic second phase for the following reasons.

(1) Microstructure analysis (XRD, SAED and HRTEM) strongly confirms one single GaN phase in samples D and E.
(2) If the segregation of the ferromagnetic compounds is too small to be detected by XRD, SAED and HRTEM measurements, they should show characteristics of superparamagnetism. The observed M–H curve for samples D and E, however, is completely different from superparamagnetism. It is typically ferromagnetic above room temperature.
(3) The lattice parameters increase as the Mn concentration increases in samples D and E (figure 1(b)), which indicates that the Mn ions have systematically substituted for the Ga ions in the lattice without changing the wurtzite structure.

At present, there is still much debate on the ferromagnetic origin of the Mn-doped III–V semiconductor materials. Some authors believe that the high-temperature intrinsic ferromagnetism originates from the GaMnN rather than the ferromagnetic second phase such as Mn_xN_y in the sample [8, 10, 19]. Zajac *et al* suggested that different Mn_xN_y phases are responsible for ferromagnetic behaviour of GaMnN with multi-phases [22]. In the next section, we will propose an explanation for the observed ferromagnetic ordering in the GaMnN nanowire samples (samples D and E) using a mean-field model based on the exchange coupling of the nondegenerate carrier-localized impurity band together with the consideration of the superexchange antiferromagnetic interaction.

4. Theoretical calculation and discussions

In spite of the recent experimental and theoretical progress, there is not yet a consensus on the physical origin leading to ferromagnetic ordering in III–V DMS materials, or a well accepted theory quantitatively explaining the ferromagnetic mechanism. Several theories, most notably Ruderman–Kittel–Kasuya–Yosida (RKKY) [23], and some extended ones based on the RKKY model in bulk semiconductors, have been used to explain the ferromagnetic phenomenon in semiconductors [1, 2, 24, 25]. All these models assume that the charge carriers (the holes) occupy the Fermi sea in the *valence band* as the result of the screening effect. This means that the free carriers contribute to the ferromagnetism in III–V compounds with degenerate holes. In such a case, the inverse Fermi wavenumber K_F^{-1} is large compared to the relevant interspin distance, so Friedel oscillation can be neglected in the indirect exchange interaction (the Zener model) [1]. However, nonzero T_c has been observed in samples with very low carrier concentration, where the chemical potential can lie within the *bandgap* instead of at the *valence band*. Furthermore, in wide-bandgap semiconductors (such as p-type Mn-doped GaN samples), hole density is not high enough to form a Fermi surface in the valence band, and the

degenerate free carrier can hardly be generated [26]. Therefore, explanation of the physical origin of the ferromagnetism in DMS based free holes is still under question. We think that the RKKY mechanism is not an ultimate model to explain the ferromagnetism in DMSs, and the high ferromagnetic transition temperature can occur in nondegenerate semiconductors. Mona Berciu *et al* proposed a bound-hole model for III–V DMSs due to the impurity band under the framework of the mean-field approximation [27]. Das Sarma *et al* calculated the magnetization in magnetically doped semiconductors, and suggested that the ferromagnetic mechanism is carrier mediated due to the formation of an impurity band [28]. Based on our experimental evidence, we can show that the fundamental mechanism underlying the observed ferromagnetism in Mn-doped GaN arises from the carrier–local spin (p–d) exchange coupling, which eventually leads to a global ferromagnetic ordering of the impurity spins for $T < T_c$, overcoming the anti-ferromagnetic or superexchange interaction between the local spins themselves. There exists very strong intrinsic disorder caused by random substitution of Mn for Ga, and strong exchange coupling between the hole and Mn spins leads to local binding of holes and Mn ions. Therefore, the impurity band induced by Mn doping in GaN is crucial to the formation of ferromagnetism. There is strong experimental evidence supporting this scenario. For example, photoemission spectroscopy revealed the existence of the impurity band in $Ga_{1-x}Mn_xAs$ with $x = 0.035$ [29]. Recent optical conductivity spectroscopy studies show the existence of impurity bands for $Ga_{1-x}Mn_xAs$ samples with $x = 0.0001$ and 0.05 [30]. In our previous study, a novel luminescence emission ($\sim$1.72 eV) was introduced in β-Ga_2O_3 nanowires via nitrogen doping, originating the recombination of an electron trapped on a donor due to oxygen vacancies and a hole trapped on an acceptor generated by nitrogen doping [16]. Detailed photoluminescence (PL) analysis of the present samples revealed that manganese doping in GaN equally introduces acceptor levels. Therefore, Mn doping introduced impurity levels play a very important role in the generation of the ferromagnetic ordering in the GaMnN DMS. We believe that the physical origin of the DMS physics is strongly related to the impurity band of the host semiconductor, in which the itinerant or the localized carriers are in extended or localized hole states in the *impurity band* rather than the *valence-band* states. The higher-energy valence-band states can be neglected in the following discussions because the spin–orbit coupling in the valence-band hole states of the III–V material plays a crucial role in the relatively disorder-free metallic systems, while our samples are most likely to be in the insulator region through the metal–insulator translation due to the low carrier concentration. Based on the above considerations, a mean-field model based on the exchange coupling of the nondegenerate carrier-localized impurity band, together with the consideration of the superexchange antiferromagnetic interaction [28], is used to calculate the magnetization of GaMnN nanowires.

The Hamiltonian in relation to our case can be written as follows [28]:

$$H = \int \mathrm{d}^3 r \sum_{\alpha} \Psi_{\alpha}^{+}(\vec{r}) \left[-\frac{\nabla^2}{2m} + V(\vec{r}) \right] \Psi_{\alpha}(\vec{r}) + \sum_{j} \int \mathrm{d}^3 r \times \left[\sum_{\alpha} W(\vec{r} - \vec{R}_j) \Psi_{\alpha}^{+}(\vec{r}) \Psi_{\alpha}(\vec{r}) + \sum_{\alpha\beta} \beta(\vec{S}_j \cdot \vec{\sigma}_{\alpha\beta}) \delta(\vec{r} - \vec{R}_j) \Psi_{\alpha}^{+}(\vec{r}) \Psi_{\beta}(\vec{r}) \right] + \sum_{j} g_i \mu_{\mathrm{B}} (\vec{S}_j \cdot \vec{H}) + \int \mathrm{d}^3 r \sum_{\alpha\beta} g_c \mu_{\mathrm{B}} \Psi_{\alpha}^{+}(\vec{r}) \Psi_{\beta}(\vec{r}) (\vec{\sigma_{\alpha\beta}} \cdot \vec{H}) \quad (1)$$

where the first term is the 'band' Hamiltonian, with m being the relevant effective mass. $V(\vec{r})$ is the random potential arising from (nonmagnetic) disorder. $W(\vec{r} - \vec{R}_j)$ is the Coulomb potential due to a magnetic impurity located at $\vec{R}_j$, and β is the p–d exchange integral. The magnetic Mn ions under consideration substitute for the Ga sites in the GaN structure, and

act both as acceptors and as magnetic impurities. In fact the electron spin resonance (ESR) analysis for sample E confirmed the existence of the A^- acceptor ($Mn^{2+}(d^5)$) with $g = 2.01$ and spin $S = 5/2$ [20]. It is noted that these values are also used in the numerical calculations in the following sections.

Under the framework of the Hamiltonian, the effective field acting upon holes has contributions from the magnetic impurities and from the external magnetic field H:

$$H_{\text{eff}}^{(c)} = \beta n_i \langle S_Z \rangle + g_c \mu_B H, \tag{2}$$

where n_i is the magnetic dopant density, g_c is the hole g factor and μ_B is the Bohr magneton. The direction of the Z axis is chosen to coincide with the direction of applied magnetic fields H, or, in the case of $H = 0$, with the direction of spontaneous magnetization of impurities. Considering the possible superexchange antiferromagnetic interaction, the effective field acting upon magnetic impurities is [28]

$$H_{\text{eff}}^{(i)} = Z^{\text{AF}} J^{\text{AF}} \langle S_Z \rangle + \beta n_c \langle s_Z \rangle + g_i \mu_B H \tag{3}$$

where J^{AF} is the antiferromagnetic exchange integral, Z^{AF} is the effective number of surrounding impurities interacting with a given impurity, n_c is the hole density and g_i is the local moment g factor.

The response of the impurity spin to this effective field $H_{\text{eff}}^{(i)}$ is given by

$$\langle S_Z \rangle = S B_s \left(\frac{S H_{\text{eff}}^{(i)}}{k_B T} \right), \tag{4}$$

$$B_s(x) = \frac{2s+1}{2s} \coth \frac{2s+1}{2s} x - \frac{1}{2s} \coth \frac{1}{2s} x \tag{5}$$

where B_s is the Brillouin function. Considering the nondegenerate model, the hole spin distribution is not affected by the Pauli exclusion principle. Therefore, the states of the electrons are determined by Boltzmann statistics. The average hole spin determined by the effective mean field $H_{\text{eff}}^{(c)}$ is given by $\langle s_Z \rangle = s B_s\left(\frac{s H_{\text{eff}}^{(c)}}{k_B T}\right)$. Using the expansion for the Brillouin functions, Curie temperature T_c is given by

$$T_c = \sqrt{T_{c0}^2 + T_1^2} - T_1 \tag{6}$$

where

$$k_B T_{c0} = \tfrac{1}{3} \beta \sqrt{n_c n_i} \sqrt{S(S+1)s(s+1)} \qquad \text{and} \qquad k_B T_1 = \tfrac{1}{6} S(S+1) Z^{\text{AF}} J^{\text{AF}}.$$

Based on this model, the magnetization of GaMnN nanowires was calculated quantitatively. What is known about DMS material is that it is a heavily compensated system, so the hole density n_c is usually just a small fraction of the magnetic dopant concentration n_i ($n_c/n_i \ll 1$) [31]. According to photoemission studies, the βN_0 for GaMnAs is $\sim 1.2 \pm 0.2$ eV [32], which means the ***p–d*** interaction is antiferromagnetic, where N_0 is the concentration of the cations. It is known that βN_0 increases with the increase of a_0^{-3}, where a_0 is the lattice constant [33]. For GaN, the value βN_0 is taken as 2.17 eV, which is evaluated from that of GaAs, in consistent with the value in [34]. The calculated T_c as a function of the hole concentration n_c for $Ga_{0.95}Mn_{0.05}N$ is shown in figure 4(a). It can be seen that $T_c = 415$ K is expected for hole concentration $n_c = 3.5 \times 10^{20}$ cm^{-3}, which is in agreement with the result of Dietl's report [1].

Study of the magnetization–temperature (M–T) relationship is very important for elucidating the physics behind DMS ferromagnetism in real systems. Figure 4(b) shows the calculated temperature dependence (M–T) of the spontaneous magnetization ($H = 0$) for $Ga_{0.95}Mn_{0.05}N$. The solid curves 1–6 correspond to different n_c/n_i values (0.01, 0.1, 0.2,

0.4, 0.6 and 0.8 respectively), and superexchange antiferromagnetic coupling is not considered ($J^{\mathrm{AF}} = 0$). It is found that the magnetization curve is very concave for samples with lower hole concentration (such as $n_c/n_i = 0.01$ and 0.1), which is different from the typical shape of conventional ferromagnetic materials. The smaller n_c/n_i, the more concave the curve shape. However, the M–T curves become convex when the density ratio n_c/n_i becomes large. In fact, the curve shape is quite close to the classical Brillouin shape for $n_c/n_i = 0.8$. When the carrier concentration is low, the system is on the insulating side of the metal–insulator transition and can be characteristic of the insulating DMS. The reason for such concave behaviour is that the effective field acting on holes is much stronger than its counterpart acting on impurities in this case. The hole magnetization reaches unity quickly below T_{c}, while the impurity magnetization is not yet fully polarized. With the increase of the hole concentration, the DMS is in the metallic region, which is characteristic of the RKKY interaction with the conventional magnetization shape. The dashed curves plotted in figure 4(b) are the magnetization curves when the superexchange antiferromagnetic coupling is taken into account. It can be seen that the antiferromagnetic coupling makes the curve very concave and further suppresses the Curie temperature of the systems.

Using the above-mentioned model, we also calculated the M–T relationship (solid curve in figure 4(c)) of sample E, and compared it with the experimental measurements (the scatter curve). The external magnetic field $H = 500$ Oe is used in the calculation, which is the same as the experimental conditions. The theoretical curve is in agreement with the experimental result in the low temperature region and has only a small deviation in the high temperature region. The calculation results in the value $n_c/n_i = 0.04$ and $Z^{\mathrm{AF}}J^{\mathrm{AF}}/\beta N_0 = 5.8 \times 10^{-4}$ for sample E. The small value of n_c/n_i reveals that the carrier concentration in the sample is low, and this is likely to be a characteristic of insulator DMSs.

It is noteworthy that the oxygen donor, codoping with the Mn acceptor in GaN, will reduce the acceptor energy level and increase the p-type carrier density, which is an advantage to the ferromagnetism in the DMS [35]. However, if the oxygen concentration is too high in the samples, like in sample A, the antiferromagnetic superexchange through the oxygen ions will suppress the Curie temperature and destroy the magnetism. It is proved through our experiments that the higher concentration of N and Mn leads to enhanced ferromagnetism in the sample.

5. Conclusions

Ferromagnetism in GaMnN nanowires was evaluated via a nitrogen doping process in Mn-doped β-Ga_2O_3 nanowires in flowing ammonia. The nitrogen concentration was controlled by the heat-treatment temperature and the product can be transformed into wurtzite GaN phase when the annealing temperature is high enough. Microstructure analysis indicates that the GaMnN nanowires have GaN wurtzite structure without Mn precipitates or Mn-related second phases. Magnetic measurement reveals that ferromagnetic ordering exists in the as-prepared GaMnN nanowires, and the Curie temperature is above room temperature. A mean-field model based on the exchange coupling of the nondegenerate carrier-localized impurity band, together with consideration of the superexchange antiferromagnetic interaction, is used to explain the physical origin of the observed ferromagnetic ordering. Theoretical calculations indicate the Curie temperature increases with the increase of hole density and reveal a small ratio of the hole to the magnetic dopant density in the samples. The low ratio of hole to Mn ion concentration and the superexchange antiferromagnetic interaction lead to the very concave temperature dependence of the magnetization curve in contrast to conventional ferromagnetic M–T behaviour. The theoretical calculation is in agreement with the experiment data.

Acknowledgments

This project is financially supported by the National Natural Science Foundation of China (grant Nos 50025206, 50472024, and 20151002), and national 973 projects (No 2002CB613505, MOST). D P Yu is supported by the Cheung Kong Scholar Programme.

References

[1] Dietl T, Ohno H, Matsukura F, Cibert J and Ferrand D 2000 *Science* **287** 1019
[2] Dietl T, Ohno H and Matsukura F 2001 *Phys. Rev.* B **63** 195205
[3] Ohno H, Shen A, Matsukura F, Oiwa A, Endo A, Katsumoto S and Iye Y 1996 *Appl. Phys. Lett.* **69** 363
[4] Ohno H, Munekata F, Penney T, Von Molnar S and Chang L L 1992 *Phys. Rev. Lett.* **68** 2664
[5] Sasaki T, Sonoda S, Yamamoto Y, Ken-ichi Suga, Shimizu S, Kindo K and Hori H 2002 *J. Appl. Phys.* **91** 7911
[6] Sharma P, Gupta A, Rao K V, Sharma R and Gehring G A 2003 *Nat. Mater.* **2** 673
[7] Matsukura F, Ohno H, Shen A and Sugawara Y 1998 *Phys. Rev.* B **57** R2037
Ohno H and Matsukura F 2001 *Solid State Commun.* **117** 179
[8] Theodoropoulou N, Hebard A F, Overberg M E, Abernathy C R, Pearton S J and Wilson R G 2001 *Appl. Phys. Lett.* **78** 3475
[9] Shon Y, Kwon Y H, Leem J H, Park C S, Fu D J, Kim H J, Kang T W and Fan X J 2002 *Appl. Phys. Lett.* **81** 1845
[10] Reed M L, El-Masry N A, Stadelmaier H H, Ritums M K, Reed M J, Parker C A, Roberts J C and Bedair S M 2001 *Appl. Phys. Lett.* **79** 3473
[11] Sonoda S, Shimizu S, Sasaki T, Yamamoto Y and Hori H 2002 *J. Cryst. Growth* **237–239** 1358
[12] Katayama-Yoshida H, Kato R and Yamamoto T 2001 *J. Cryst. Growth* **231** 428
[13] Ohno H 1998 *Science* **281** 951
[14] Thaler G, Frazier R, Gila B, Stapleton J, Abernathy C R, Pearton S J and Segre C 2004 *Appl. Phys. Lett.* **84** 1314
[15] Deepak F L, Vanitha P U, Fovindaraj A and Rao C N R 2003 *Chem. Phys. Lett.* **374** 314
[16] Song Y P, Zhang H Z, Lin C, Zhu Y W, Li G H, Yang F H and Yu D P 2004 *Phys. Rev.* B **69** 075304
[17] Wang P W, Song Y P, Wang Z and Yu D P 2004 unpublished
[18] Zhang H Z, Kong Y C, Wang Y Z, Du X, Bai Z G, Wang J J and Yu D P 1999 *Solid State Commun.* **109** 677
[19] Overberg M E, Abernathy C R, Pearton S J, Theodoropoulou N A, McCarthy K T and Hebard A F 2001 *Appl. Phys. Lett.* **79** 1312
[20] Zajac M, Doradzinski R, Szczytko J, Lefeld-Sosnowska M, Kaminska M, Twardowski A, Palczewska M, Grzanka E and Gebicki W 2001 *Appl. Phys. Lett.* **78** 1276
[21] Guillermet A F and Grimvall G 1989 *Phys. Rev.* B **40** 10582
[22] Zajac M, Gosk J, Grzanka E, Kaminska M, Twardowski A, Strojek B, Szyszko T and Podsiadło S 2003 *J. Appl. Phys.* **93** 4715
[23] Dietl T, Haury A and d'Aubigne Y M 1997 *Phys. Rev.* B **55** R3347
Matsukura F, Ohno H, Shen A and Sugawara Y 1998 *Phys. Rev.* B **57** R2037
[24] Lee B H, Jungwirth T and Macdonald A H 2000 *Phys. Rev.* B **61** 15606
[25] Boselli M A and Ghazali A 2000 *Phys. Rev.* B **62** 8895
[26] Akinaga H, Nemeth S, De Boeck J, Nistor L, Bender H and Borghs G 2000 *Appl. Phys. Lett.* **77** 4377
[27] Berciu M and Bhatt R N 2004 *Phys. Rev.* B **69** 045202
[28] Das Sarma S, Hwang E H and Kaminski A 2003 *Phys. Rev.* B **67** 155201
[29] Okabayashi J, Kimura A, Rader O, Mizokawa T, Fujimori A, Hayashi T and Tanaka M 2001 *Physica* E **10** 192
[30] Singley E J, Kawakami R, Awschalom D D and Basov D N 2002 *Phys. Rev. Lett.* **89** 097203
[31] Beschoten B, Crowell P A, Malajovich I, Awschalom D D, Matsukura F, Shen A and Ohno H 1999 *Phys. Rev. Lett.* **83** 3073
[32] Okabayashi J, Kimura A, Rader O, Mizokawa T, Fujimori A, Hayashi T and Tanaka M 1998 *Phys. Rev.* B **58** R4211
[33] Furdyna J K 1988 *J. Appl. Phys.* **64** R29
Stolpe I 1998 *Physica* B **256–258** 659
[34] Dietl T, Matsukura F and Ohno H 2002 *Phys. Rev.* B **66** 033203
[35] Katayama-Yoshida H, Kato R and Yamamoto T 2001 *J. Cryst. Growth* **231** 428
Korotkov R Y, Gregie J M and Wessels B W 2001 *Appl. Phys. Lett.* **78** 222